

5 6 **Optimum Asymmetric Spatial and Temporal Distribution of** 7 **Femtosecond Laser Pulses in Refractive Surgery**

8 Samuel Arba Mosquera^{1*}, Shwetabh Verma^{1*}

9 ¹ SCHWIND eye-tech-solutions GmbH, Research and Development, Kleinostheim D-63801, Germany

10 **Abstract** – Femtosecond laser–assisted refractive correction relies on temporally and spatially separated pulses that
11 generate coalescent cavitation bubbles, forming a cleavage plane for tissue separation. Achieving optimal outcomes
12 requires balancing laser-induced stress, mechanical dissection stress, and surface roughness. This work introduces a
13 nonlinear absorption model and a theoretical framework to identify the optimum spatial and temporal distribution of
14 single pulses. The analysis, based on inequalities involving scaling factors for spot size and track distance, defines a
15 bounded solution space. Within this domain, the most favorable setting corresponds to minimum dose with maximum
16 asymmetry, ensuring energy efficiency while enhancing surface smoothness, whereas the least advantageous of the
17 optimum conditions occurs for higher dose and minimum asymmetry (compatible with optimum conditions) both
18 enabling a theoretical bridge-free dissection. Bubble overlap emerges as a key determinant of cutting efficiency and
19 smoothness, and an optimal window for overlap factors is delineated, minimizing treatment dose while preserving
20 corneal quality through smoother stromal cuts.

21 **Keywords:** Asymmetric spacing, Spatial and Temporal Pulse Distribution, Dose optimization, Surface smoothness,
22 Femtosecond laser, Refractive Surgery.

23 **1. Introduction**

24 Refractive surgery has advanced with the introduction of ultrashort-pulse laser systems^{1,2}. Under high concentrated peak
25 irradiances and shorter exposure times, in the picosecond and femtosecond (fs) range, one can not only break molecules as
26 during photoablation, but even strip electrons from their atoms and accelerate them resulting in generation of dense free
27 electron plasma. If a critical value is exceeded, laser induced optical breakdown (LIOB) occurs with very fast increase of
28 temperature and pressure, which leads to a rapid plasma expansion. This results in a shock wave propagating into the
29 surrounding medium, causing the formation of a cavitation bubble, which may undergo a series of oscillations before ending in
30 a small persistent gas bubble after some microseconds. Plasma-mediated ablation^{3,4} and photodisruption^{5,6} are the key laser–
31 tissue interaction mechanisms underlying femtosecond laser–assisted techniques, enabling precise intrastromal dissection. In
32 Photodisruption, microjoule-range pulses at high repetition rates and micrometer-scale spacing create cavitation bubbles that
33 mechanically separate stromal lamellae, whereas in plasma-mediated ablation, lower pulse energies delivered at multi-MHz
34 rates with strong pulse overlap result in tissue separation through cumulative free-electron–mediated effects without cavitation.
35 The (asymptotic) size of the cavitation bubble leading to photodisruption grows with the cubic root of the applied
36 (suprathreshold) pulse energy^{7,8}. Theoretical models and empirical data have substantiated the importance of identifying the
37 fine differences between the two interaction mechanisms to explain the cavitation bubble dynamics and reliably estimating its
38 size at any given single pulse energy⁹.

39 Femtosecond lasers generate plasma and cavitation bubbles with substantially lower energy thresholds than longer-pulse
40 systems due to nonlinear multiphoton absorption¹⁰. In corneal tissue, femtosecond optical breakdown typically occurs at pulse
41 energies on the order of tens to hundreds of nanojoules, depending on numerical aperture, pulse duration, and tissue hydration,
42 with reported breakdown thresholds in the range of approximately 25–200 nJ for commonly used clinical focusing
43 conditions^{10–12}. The resulting cavitation bubbles in intrastromal corneal surgery exhibit characteristic radii typically in the
44 range of 0.7–3 μm , with upper clinical values approaching 4–5 μm at higher pulse energies^{13–15}. Clinical systems generally

* Corresponding authors: Samuel.Arba.Mosquera@eye-tech.net and shwetabh.verma@yahoo.com

45 avoid pulse energies that generate bubbles exceeding $\sim 5 \mu\text{m}$ radius due to the increased risk of stromal disruption, endothelial
46 stress, and irregular interface formation¹⁶.

47 The affected diameter of a single spot is typically on the order of $1\text{--}10 \mu\text{m}$, whereas the treatment zone diameter ranges
48 from $6\text{--}9 \text{mm}$, yielding a scale separation exceeding three orders of magnitude^{15,17}. Because of this extreme scale separation,
49 the corneal surface may be regarded as locally planar both radially and azimuthally, independent of whether the global scan
50 pattern is spiral, raster, or meander. Thus, the local geometry governing bubble overlap is effectively Cartesian.

51 Due to the scale separation, multiple laser pulses are sequentially delivered on to the cornea. Each laser pulse locally
52 creates a small cavitation bubble separating the corneal tissue. The global process is an integral effect of the local process of
53 each individual laser pulse. A larger bubble gives a faster treatment, but a lower resolution. On the other hand, a smaller bubble
54 increases the resolution at the cost of increasing the treatment time due to increased number of laser pulses invested in cutting
55 the same area. Additionally, using laser pulses too close to the threshold of the material (for generating cavitation bubbles)
56 would mean only imparting thermal effects instead of generating stable bubbles. All these factors make the energy selection a
57 sensitive criterion.

58 The laser pulses in femtosecond laser-assisted refractive correction techniques are separated both spatially (spot and track
59 separation conforming a pattern, Fig. 1) and temporally (pulse repetition rate, and track frequency). The spatially and
60 temporally scanned process eventually leads to a confluent (or coalescent) bubble (conforming a cleavage plane), enabling the
61 separation of the tissue. The residual tissue bridges between cavitation sites have a significant clinical relevance. Histological
62 and surgical experience suggests that residual tissue bridges remaining after femtosecond laser lamellar ablation are associated
63 with increased interface roughness and less smooth cleavage surfaces; when the uncut gaps between cavitation sites approach a
64 significant fraction of the cavitation bubble diameter, surface irregularities become more pronounced^{18,19}. While precise
65 clinical thresholds are not universally defined, surgical practice suggests residual gaps larger than a few microns can influence
66 interface smoothness and biomechanical stability postoperatively.

67 Individual pulses and cumulative effects may be governed by different underlying mechanisms. For instance, very different
68 regimes have been observed for the interaction mechanisms of cavitation bubbles induced by spatially and temporally
69 separated fs-laser pulses (at least for pulse energies well above the breakdown threshold)^{20,21}. Tinne et. al.^{8,17} first
70 investigated the interaction mechanisms of cavitation bubbles induced by two laser pulses that were both spatially and
71 temporally separated. In a more recent study, Freidank et al.¹⁵ presented high-speed videographic investigations performed at
72 up to 50 million frames per second, of multiple pulse effects during intrastromal dissection in corneal tissue. They found that
73 the bubble dynamics in corneal tissue are much more complex than in water. The laser-induced bubbles exist longer in tissue
74 and are not spherical, instead multiple bubble lobes are formed along the elongated laser plasma within the cornea. These lobes
75 expand preferentially along the corneal lamellae, which are approximately $2\text{--}3 \mu\text{m}$ thick, creating overlapping layers of
76 bubbles aligned with the stromal architecture suggesting that spot spacing and pulse overlap, both in depth and across lamellae,
77 play a critical role in determining whether the resulting cut is smooth or fragmented.

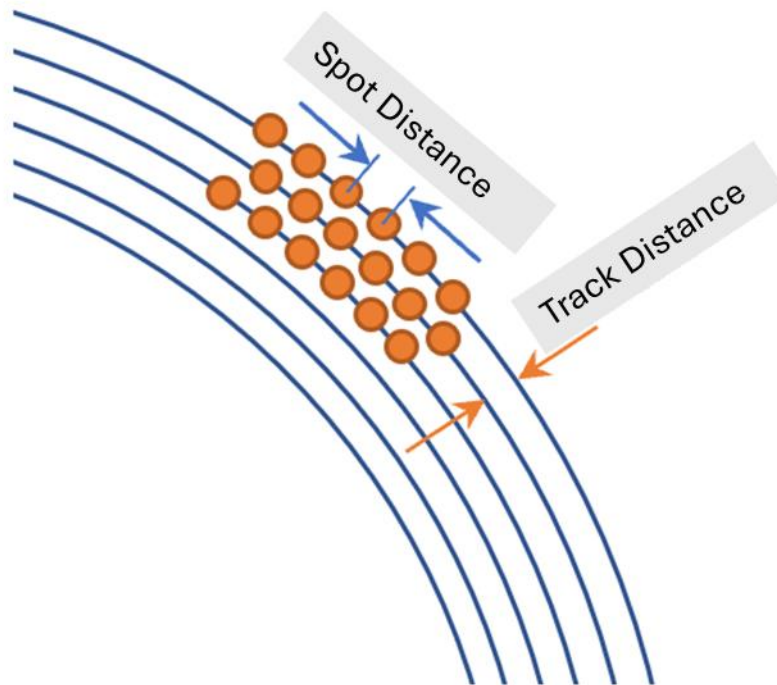


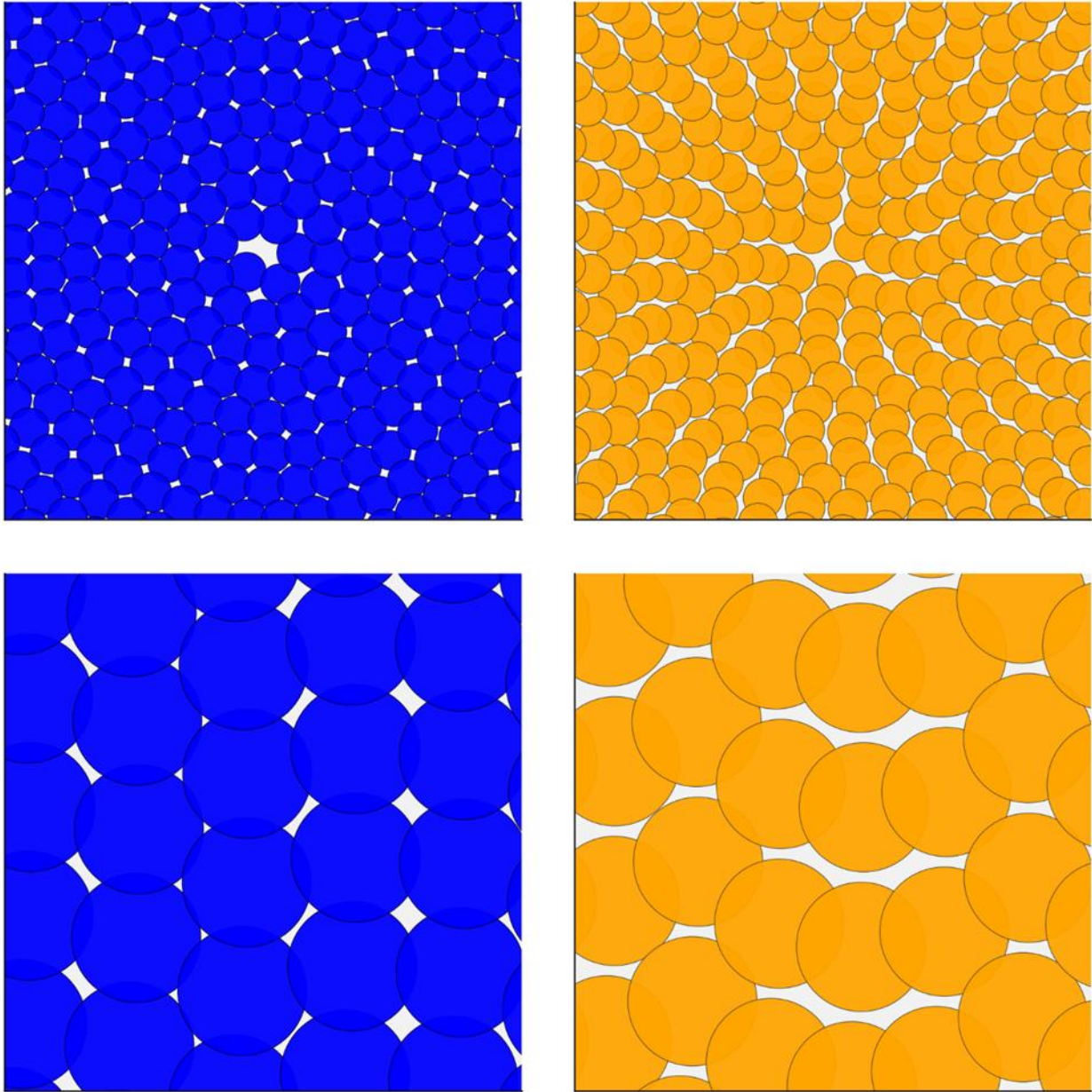
Fig. 1 Illustrative representation of the spatial distribution of cavitation bubbles determined by spot and track distances in femtosecond laser–assisted refractive correction.

Several studies have investigated the impact of optimizing pulse energy, and temporal and spatial relationships between single pulses. Adapting the laser settings in femtosecond laser-assisted cataract surgery with increased vertical spacing (i.e. fewer pulses in vertical direction) has shown to significantly reduce the number and size of “tags” (incomplete / misplaced cuts) at the capsule edge, thereby improving the cut quality²². Lombardo et al.²³ investigated morphology of posterior stromal lenticles created with a femtosecond laser. Their results showed that lower pulse energy (0.50 μJ) produced much smoother posterior stromal lenticle surfaces while roughness increased with increasing energy. Very fine spot spacing (2 μm) with low energy resulted in surface comparable to mechanical microkeratome. In the study by Amann & Arba-Mosquera²⁴, the authors conducted detailed simulations of femtosecond LIOB to assess how variations in spot spacing and track spacing influence corneal surface roughness. Their optimization framework consistently favored asymmetric spacing patterns, delivered at laser energies just above the LIOB threshold, to reduce surface irregularities.

In this regard and at least in the context of this work, we use the terminology symmetric vs. asymmetric spacings respect to spot and track distances, as well as asymmetry ratio, according to previous publications²⁴. Figures 2 provide a visual representation of symmetric and asymmetric pulse spacings respectively. Symmetric spacings refer to conditions in which spot distance (Fig. 1 and 2) along the pathway (azimuthal in rotational scanning approaches and linear in meander scanning approaches) equals the track distance (Fig. 1 and 2) across the pathway (radial in rotational scanning approaches and line-wise in meander scanning approaches), this leads to an asymmetry ratio of 1. By exclusion, asymmetric spacings refer to conditions in which spot and track distances (Fig. 1 and 2) along and across the pathway, respectively, are different, this leads to an asymmetry ratio different from 1. Geometrically it would make no difference which one is higher (yet physically and spatiotemporally), so that we only explored asymmetry ratios >1 (also as per previous publications²⁴), i.e. in which the spot distance (Fig. 1 and 2) along the pathway is clearly larger than the track distance (Fig. 1 and 2) across the pathway.

The understanding of underlying mechanisms of distribution of laser pulses and their impact on outcomes may help optimize refractive laser systems. Symmetric spacing produces a regular, structured pattern in which the selected spot and track distances typically yield a low to moderate energy dose, resulting in a standard dissection. In contrast, asymmetric spacing

105 arises from a stochastic pulse distribution that, when appropriately configured, can achieve a lower effective dose and
106 influence the characteristics of tissue separation.
107



108
109 **Fig. 2** Visual representation of symmetric pulse spacing (left) and asymmetric spacing (right) on an Archimedean spiral, shown
110 at different zoom levels for the central region (top) and peripheral region (bottom). For symmetric spacing, the bubble
111 boundary is shown as a black contour with blue fill; for asymmetric spacing, the bubble boundary is shown as a grey contour
112 with orange fill.
113

114 In previous works we presented analytical models to optimize the laser settings of ablation processes governed by linear²⁵
115 and non-linear (multi-photon) absorption²⁶. The main purpose of this paper is to extend the non-linear absorption model and
116 present a simple theoretical framework for identifying the optimum spatial and temporal distribution of single pulses for
117 maximizing the cutting efficiency defined by the metrics minimum amount of energy imparted to the tissue (i.e. minimum
118 dose) and minimum corneal surface roughness.

Please note that this work does not aim to reduce cavitation energy to a level slightly above the threshold, as explored in previous studies^{9,26}. Instead, the objective is to provide a simplified theoretical framework for objectively determining:

- the optimum total energy or dose appropriate for a given treatment or laser system, and
- the optimum degree of asymmetry (spatial or temporal) corresponding to that total energy/dose for the same treatment or system.

The femtosecond laser cavitation bubble expansion and collapse remain highly confined compared to the overall treatment diameter which can be several millimetres, which justifies the local geometric modelling assumptions employed in this work.

2. Material and Methods

2.1. Calculation of the overall dose per treatment

The dose, or total fluence, in refractive laser surgery is defined as the average energy delivered per unit surface area of the treated corneal region. Because each laser pulse within a given cut is delivered with a constant energy level (though this may vary between cuts within a treatment), the dose effectively reflects the pulse density, that is, the number of pulses delivered per unit area.

The following equation applies for the calculation of the overall dose per treatment D_T ²⁶

$$D_T = \frac{E_T}{A_T} \quad (1)$$

$$D_T = \frac{n \cdot E_P}{\pi \cdot R_T^2} \quad (2)$$

where E_T is the total energy deposited during a treatment, E_P is the energy of a single pulse, A_T is the area of the treatment and R_T its radius. The number ' n ' represents the number of pulses assuming that all pulses carry the same energy, and pulses are approximately evenly distributed in the treatment area.

The total number of pulses delivered can be estimated geometrically. Assuming pulses are distributed in concentric circular paths (laps), the total number of laps and the average lap radius can be used to calculate the path length. This path length when divided by the spot distance gives the total number of pulses (for a single pass over the treatment area) as follows²⁶:

$$n = \frac{\pi \cdot R_T^2}{\text{Spot Distance} \cdot \text{Track Distance}} \quad (3)$$

where *Spot Distances* and *Track Distance* are distances between deposited neighboring spots along two essentially perpendicular axes (e.g. x and y but also r and θ).

Therewith, the overall dose per treatment simplifies to:

$$D_T = \frac{E_P}{\text{Spot Distance} \cdot \text{Track Distance}} \quad (4)$$

This expression shows that the *Dose* is independent of treatment area and is solely a function of pulse energy and spatial pulse density. The product of *Spot Distance* · *Track Distance* can be interpreted as the effective area assigned to each pulse, rather than the physical bubble size itself.

On the other hand, the lower limit (minimum) dose (D_{min}) per treatment for a bridge-free dissection can be equated as:

$$D_{min} = \frac{E_P}{\text{Bubble Area}} = \frac{E_P}{\pi \cdot R_B^2} \quad (5)$$

This expression shows that the minimum dose is a function of pulse energy and bubble area, i.e. limited by the physical bubble size itself.

In this work, the terms "*Bubble Area*" and "*Bubble Diameter*" actually refer to the tissue disruption size (area or diameter) caused by a single bubble. It is not a time-dependent quantity since it refers to the effective size once the bubble completes the disruption work, thus it requires the bubble already collapsed in time after creating the disruption effect. Therefore, the *Bubble Area* refers to the planar projection of the cavitation bubble onto the cut surface, not the total bubble surface. In a 3D lattice, each Voronoi cell is formed by 4 or 6 neighboring spots, which occupy a very small spatial window relative to corneal

curvature. Hence, the cornea is locally planar in 3D over each cell²⁴. Therefore, local curvature effects are negligible at the scale of individual Voronoi cells, and global corneal curvature does not influence the local overlap statistics used in the model, justifying that scanning pattern geometry (spiral, raster, etc.) does not alter the local overlap physics, allowing the problem to be treated in a locally Cartesian framework.

2.2. Calculation of the overall dose per treatment as a function of scaling factors for Spot and Track Distance

Considering a scaling factor ' F ' that is dimensionless and affects spacing relative to bubble size, one can calculate the *Spot* and *track distance* with respect to *Bubble Diameter* as follows:

$$\text{Spot Distance} = \frac{\text{Bubble Diameter}}{F_1} \quad (6)$$

$$\text{Track Distance} = \frac{\text{Bubble Diameter}}{F_2} \quad (7)$$

Where F_1 and F_2 are scaling factors for *Spot* and *Track Distance* respectively, and in general values F_1 or $F_2 > 1$ represent effective spot or track overlap, and values F_1 or $F_2 < 1$ actually suggest disjoint spot or track cumulation. Therefore, if F_1 and F_2 are large, the *Spot* and *Track Distances* would be a small fraction of *Bubble Diameter*, resulting in more overlap, higher number of pulses per area and a higher dose, resulting potentially in a clean cut. Conversely, if F_1 and F_2 are small, the *Spot* and *Track Distances* may become large multiples of *Bubble Diameter*, resulting in less to no overlap, lower dose but may pose a higher risk of incomplete cut.

Using Eq. 4, and applying Eq. 6 and 7, D_T can be expressed as follows:

$$D_T = \frac{E_p \cdot F_1 \cdot F_2}{\text{Bubble Diameter}^2} \quad (8)$$

2.3. Calculation of optimum window for Spot and Track Distance

The bubble overlap denoted by the scaling factors F_1 and F_2 plays a pivotal role in determining cutting smoothness and efficiency. We extend our previous works^{24,26} to define an optimum window for the overlap factors that minimizes overall dose per treatment and corneal surface roughness.

Numerical simulations and graphical visualizations of overlapping disk geometries presented in the Results were generated using Python (CPython implementation) in a Jupyter-based execution environment provided by OpenAI, employing standard scientific libraries including NumPy, SciPy, and Matplotlib.

3. Results

3.1. Minimum Overall Dose per treatment

Following Eq. 5, the Minimum Overall Dose per treatment (D_{min}) is related to energy of a single pulse (E_p), Area of a single cavitation bubble (*Bubble Area*) and *Bubble Diameter* as follows:

$$\text{Bubble Area} = \frac{\pi \cdot \text{Bubble Diameter}^2}{4} \quad (9)$$

$$D_{Min} = \frac{E_p \cdot \left(\frac{4}{\pi}\right)}{\text{Bubble Diameter}^2} \quad (10)$$

This is the Minimum Overall Dose per treatment (D_{min}) since using a lower number of pulses (ie, smaller $F1 \cdot F2$ product) (all leading to that bubble area) would always result in tissue bridges (since the *Bubble Area* · *number of pulses* would be smaller than the treatment area).

Comparing Eq. 10 and Eq. 8, the term for scaling factors for *Spot* and *Track Distance* for this Dose (D_{Min}) should be as follows:

$$F1 \cdot F2 \geq \left(\frac{4}{\pi}\right) \quad (11)$$

3.2. Maximum required Overall Dose per treatment

As shown in our previous works²⁶, the spot and track distance for which adjacent bubbles would largely overlap in the two principal directions and just overlap in the two diagonal directions leaving no tissue bridges, can be calculated as follows:

$$Spot \ Distance = \frac{Bubble \ Diameter}{2^{0.5}} \quad (12)$$

$$Track \ Distance = \frac{Bubble \ Diameter}{2^{0.5}} \quad (13)$$

From Eq 8 combined with Eqs 12 and 13, the maximum required Dose (D_{Max}) for this Spot and Track Distance is:

$$D_{Max} = \frac{E_P \cdot 2}{Bubble \ Diameter^2} \quad (14)$$

Comparing Eq. 14 and Eq. 8, the term for scaling factors for *Spot* and *Track Distance* from this Dose (D_{Max}) should be as follows:

$$F1 \cdot F2 \leq 2 \quad (15)$$

This is the Maximum required Overall Dose per treatment (D_{Max}) since using a greater number of pulses (ie, larger $F1 \cdot F2$ product) (all leading to that *Bubble Area*) would result in tighter bubble overlap without reducing the amount of tissue bridges (since for $F1 \cdot F2 = 2$, adjacent bubbles would largely overlap in the two principal directions and just overlap in the two diagonal directions leaving no tissue bridges).

Figure 3 visually illustrates the impact of the product of scaling factors $F1$ and $F2$.

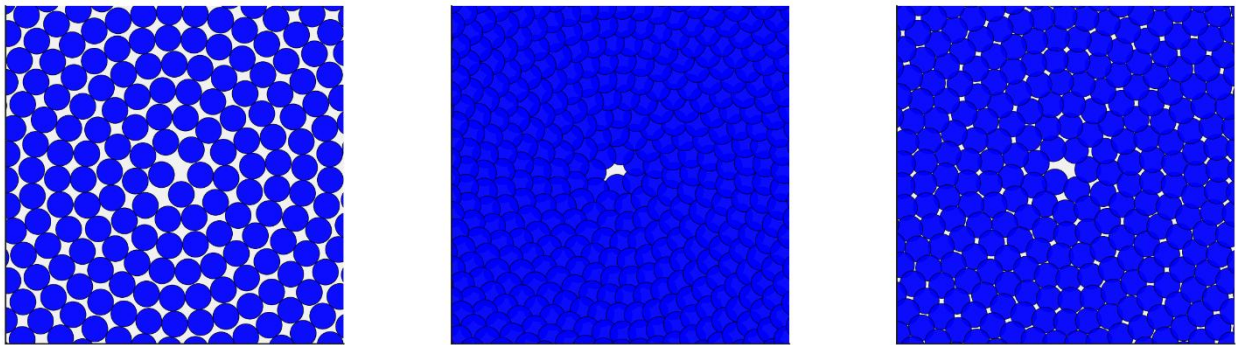


Fig. 3 Visual representation of symmetric pulse spacing ($F1 = F2$) on an Archimedean spiral, shown for different values of the product of scaling factors $F1$ and $F2$. Left: $F1 \cdot F2 = 1$, adjacent bubbles do not overlap in the two principal directions and diagonal directions leaving tissue bridges. Middle: $F1 \cdot F2 = 2$, adjacent bubbles largely overlap in the two principal directions and just overlap in the two diagonal directions leaving no tissue bridges. Right: $F1 \cdot F2 = 1.41$, A good compromise that enables tissue bridge-free bubble overlap while minimizing the dose.

A window for scaling factors can be estimated comparing the Minimum and Maximum Dose terms (Eq. 11 and Eq. 15):

$$\left(\frac{4}{\pi}\right) \leq F1 \cdot F2 \leq 2 \quad (16)$$

246
247
248
249
250
251
252
253
254
255
256
257
258
259
260
261

In the clinical context, the typical values of $F1$ and $F2$ are confined within upper and lower bounds. From both geometric necessity and clinical experience, meaningful contiguous cutting requires $F_{1,2} > \frac{2}{\sqrt{\pi}} \approx 1.13$, which corresponds to the minimum spacing for planar area coverage by circular projections. Practical clinical limits are typically $F_{1,2} < \sqrt{2} \approx 1.41$, which allows not very dense placement which can cause excessive mechanical disruption, although some commercial systems exceed this in specific protocols. In symmetric configurations, typical clinical values often fall in the range $F_{1,2} \approx 2^{1/4}$ to $2^{1/2}$, corresponding to efficient overlap with limited energy redundancy²⁴. Modern clinical systems increasingly employ $F1 \neq F2$, for example to optimize cut smoothness as simulations suggest that lower pulse energies (well above the LIOB threshold) combined with asymmetric spacings (spot-to-track distance ratio $\gg 1$) may be effective to lower the roughness of laser cuts²⁴, such that the ratio of $F2/F1$ should be:

$$F1 > F2 \quad (17)$$

$$\frac{2}{\sqrt{3}} \leq \frac{F2}{F1} \leq 2 \cdot \sqrt{3} \quad (18)$$

Representative numerical ranges are included in the examples below to make these quantities interpretable in practice.

262

3.3. Optimum window for Spot and Track Distance

263
264
265
266
267
268
269
270
271
272
273
274

From the two inequalities presented in Eq. (16) and Eq. (18), involving the scaling factors for Spot ($F1$) and Track Distance ($F2$), a bounded solution space can be defined (Table 1).

The feasible region is delimited by the minimum and maximum values of the product $F1 \cdot F2$ (dose) and the ratio $F2/F1$ (asymmetry). This rectangular domain naturally gives rise to four corner solutions, each representing an extreme combination of dose and asymmetry (Fig. 4). Among these, the most favorable setting is located at the corner of minimum dose and maximum asymmetry, which combines energy efficiency with smoother cuts. Conversely, the least desirable region corresponds to the corner of maximum dose and minimum asymmetry, which should be avoided. The optimal operating point therefore lies toward the lower-right corner of the solution space. The two intersecting lines highlight intermediate trade-offs: the vertical line represents moderate asymmetry across the full dose range, while the horizontal line represents moderate dose across the full asymmetry range. From this cross-section, a Proper Optimum was derived as the geometric mean of the vertical and horizontal solutions, lying near Solution 4. This calculated optimum (as indicated in Fig. 4) corresponds to an asymmetry of $F2/F1=2.63$ and a dose of $F1 \cdot F2=1.41$.

275
276
277

Table. 1 Corner solutions derived from the inequalities (Eqs. (16) and (18)). Each solution represents an extreme case of dose and asymmetry. The optimum lies at minimum dose with maximum asymmetry, whereas the combination of moderate dose and minimum asymmetry is the least advantageous of the optimum solutions.

Solution	Dose ($F1 \cdot F2$)	Asymmetry ($F2/F1$)	Interpretation
1	2 (Maximum)	$2/\sqrt{3}$ (low)	moderate dose, low asymmetry $F1 \cdot F2=2$ ensures tissue bridge-free bubble overlap $F2/F1=2/\sqrt{3}$ is the smallest asymmetry of a hexagonal lattice
2	$4/\pi$ (Minimum)	$2/\sqrt{3}$ (low)	minimum dose, low asymmetry $F1 \cdot F2=4/\pi$ enables tissue bridge-free bubble overlap with minimum dose $F2/F1=2/\sqrt{3}$ is the smallest asymmetry of a hexagonal lattice
3	2 (Maximum)	$2\sqrt{3}$ (high)	moderate dose, high asymmetry (lower roughness) $F1 \cdot F2=2$ ensures tissue bridge-free bubble overlap $F2/F1=2\sqrt{3}$ is the largest asymmetry of a hexagonal lattice
4	$4/\pi$ (Minimum)	$2\sqrt{3}$ (high)	minimum dose, high asymmetry (lower roughness) $F1 \cdot F2=4/\pi$ enables tissue bridge-free bubble overlap with minimum dose $F2/F1=2\sqrt{3}$ is the largest asymmetry of a hexagonal lattice

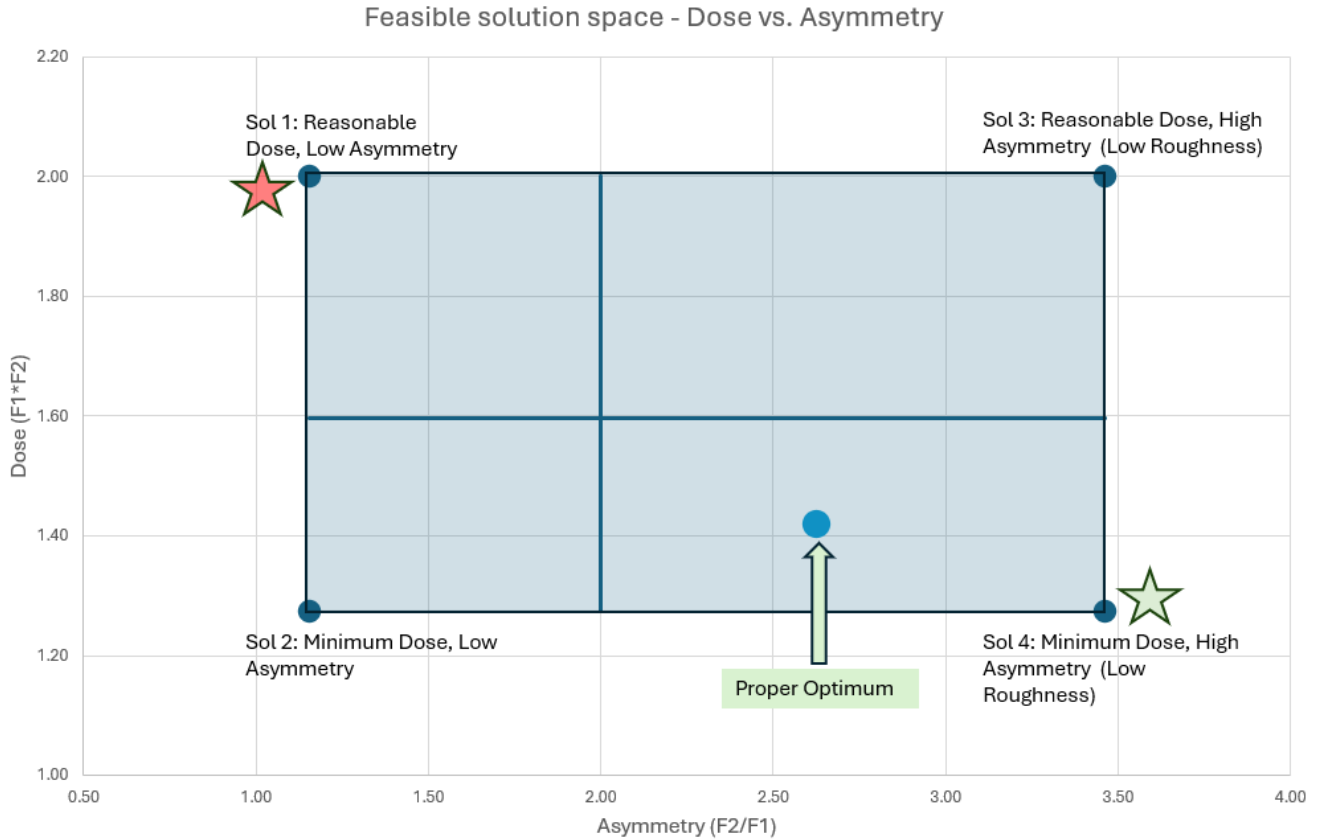


Fig. 4 Feasible solution space defined by inequalities (Eqs. (16) and (18)). The rectangle represents the bounded domain of dose ($F1 \cdot F2$) and asymmetry ($F2/F1$). The four corner points correspond to extreme combinations. The most favorable setting is found at minimum dose and maximum asymmetry (Indicated with a Green star), while the least desirable of the optimum conditions is at maximum dose and minimum asymmetry (indicated with a Red star). The vertical and horizontal lines illustrate intermediate trade-offs across dose and asymmetry, from which a proper optimum is derived (blue marker), located near Solution 4.

In addition to the four corner solutions derived from the inequalities (Eqs. (16) and (18)) representing extreme case of dose and asymmetry, the case of $F1=1$ was also evaluated. The corresponding values of $F1$ and $F2$ for these combinations are summarized in Table 2, while the resulting ranges of $F1$ and $F2$ are provided in Table 3.

Table. 2 Values of $F1$ and $F2$ corresponding to the four corner solutions defined by the inequalities (Eqs. (16) and (18)), together with the additional case $F1=1$.

$F1 \cdot F2$	$F2/F1$	$F1$	$F2$
1.27	3.46	0.61	2.10
2.00	3.46	0.76	2.63
1.27	1.15	1.05	1.21
2.00	1.15	1.32	1.52
1.27	1.27	1.00	1.27
2.00	2.00	1.00	2.00

Table. 3 Calculated Maximum and Minimum ranges for $F1$ and $F2$.

	$F1$	$F2$
min	0.61	1.21
MAX	1.32	2.63

293
294
295
296

Following the Photodisruption model⁹, and using the different exemplary combinations of dose ($F1 \cdot F2$) and Asymmetry ($F2/F1$), the *Spot Distance*, *Track Distance* and corresponding dose for each combination is calculated for a particular LIOB threshold ($E_{th} = 50\text{nJ}$) and Single Pulse Energy ($E_p = 100\text{nJ}$), and presented in Table 4.

297
298

Table. 4 *Spot Distance*, *Track Distance* and *Dose* calculated for different exemplary combinations of dose ($F1 \cdot F2$) and asymmetry ($F2/F1$) for a particular LIOB Threshold Energy (50nJ) and Single pulse energy ($E_p = 100\text{nJ}$).

$F1 \cdot F2$	$F2/F1$	$F1$	$F2$	E_{th} (nJ)	E_p (nJ)	Bubble Diameter (μm)	Spot Distance (μm)	Track Distance (μm)	Dose (mJ/cm^2)
1.27	1.27	1.00	1.27	50	100	5.3	5.3	4.2	446
1.43	1.60	0.95	1.51	50	100	5.3	5.7	3.5	500
1.60	2.00	0.89	1.79	50	100	5.3	6.0	3.0	559
1.79	2.63	0.82	2.17	50	100	5.3	6.5	2.5	626
2.00	3.46	0.76	2.63	50	100	5.3	7.0	2.0	701

299
300
301
302
303

Using LIOB Threshold energies loosely representing commercial systems currently used in ultrashort-pulse corneal tissue cutting, and the calculated optimum Single Pulse Energies compatible with previous works⁹, for the different exemplary combinations of a proper optimum for dose ($F1 \cdot F2$) and Asymmetry ($F2/F1$), the *Spot Distance*, *Track Distance* and corresponding *Dose* is presented in Table 5.

304
305

Table. 5 *Spot Distance*, *Track Distance* and *Dose* calculated for different exemplary combinations of dose ($F1 \cdot F2$) and asymmetry ($F2/F1$) for a series of LIOB Threshold Energy and pulse energies compatible with previous works⁹.

$F1 \cdot F2$	$F2/F1$	$F1$	$F2$	E_{th} (nJ)	E_p (nJ)	Bubble Diameter (μm)	Spot Distance (μm)	Track Distance (μm)	Dose (mJ/cm^2)
1.41	2.62	0.73	1.92	35	50	3.6	4.9	1.9	553
1.41	2.62	0.73	1.92	35	70	4.7	6.5	2.5	440
1.41	2.62	0.73	1.92	35	100	5.8	7.9	3.0	416
1.41	2.62	0.73	1.92	50	70	3.9	5.4	2.0	639
1.41	2.62	0.73	1.92	50	100	5.3	7.3	2.8	496
1.41	2.62	0.73	1.92	50	145	6.6	9.0	3.4	468
1.41	2.62	0.73	1.92	70	100	4.5	6.1	2.3	697
1.41	2.62	0.73	1.92	70	145	6.1	8.3	3.2	548
1.41	2.62	0.73	1.92	70	200	7.3	10.0	3.8	524

306
307
308
309
310

In Table 5, three different laser-induced optical breakdown (LIOB) threshold energies ($E_{th} = 35\text{ nJ}$, 50 nJ , and 70 nJ) were analyzed, which loosely represent the range of commercial femtosecond laser systems currently applied for ultrashort-pulse corneal tissue cutting. For each threshold energy, three different single-pulse energies (E_p) were evaluated. The selection of E_{th} values follows the rationale established in our previous work⁹.

311
312
313
314
315
316
317
318

The first E_p for each E_{th} was set at approximately $1.4 \cdot E_{th}$, corresponding to the minimum optimum predicted by the PlasmaCRT model ($\exp(1/3) \cdot E_{th}$). The second E_p was set at approximately $2 \cdot E_{th}$, representing the maximum optimum from the PlasmaCRT model ($\exp(2/3) \cdot E_{th}$), while also coinciding with the proper optimum predicted by the Photodisruption model. The third E_p was set at approximately $3 \cdot E_{th}$, nearly aligning with the maximum optima from both the Photodisruption and PlasmaSQR models ($\exp(1) \cdot E_{th}$). This design also allows direct cross-comparison of specific E_p values across categories: for example, 70 nJ and 100 nJ were tested at both $E_{th} = 35\text{ nJ}$ and $E_{th} = 50\text{ nJ}$, while 100 nJ and 145 nJ were tested at both $E_{th} = 50\text{ nJ}$ and $E_{th} = 70\text{ nJ}$. In addition, $E_p = 100\text{ nJ}$ was included in all three categories to explicitly demonstrate the effect of varying threshold energy on outcomes at a constant single-pulse energy.

319
320

4. Discussion

321
322
323
324
325
326
327
328

The bubble overlap plays a pivotal role in determining cutting smoothness and efficiency. There is no strict requirement for spot spacing to be smaller than the cavitation bubble diameter because effective tissue dissection in femtosecond laser procedures depends not solely on overlap along the scanning path (governed by spot spacing), but on the overall spatial and temporal interaction of cavitation bubbles, which is jointly determined by spot and track spacing. In this work, we defined universal ranges for $F1$ and $F2$ in relation to *spot* and *track distances*, where F represents the scaling factor relative to bubble size. As demonstrated in Tables 2 to 5, $F1$ (the scaling factor for spot distance) is consistently below unity under most conditions, indicating little to no overlap along the spot pathway. In contrast, $F2$ (the scaling factor for track distance) remains consistently greater than one, reflecting a stronger degree of overlap between adjacent tracks.

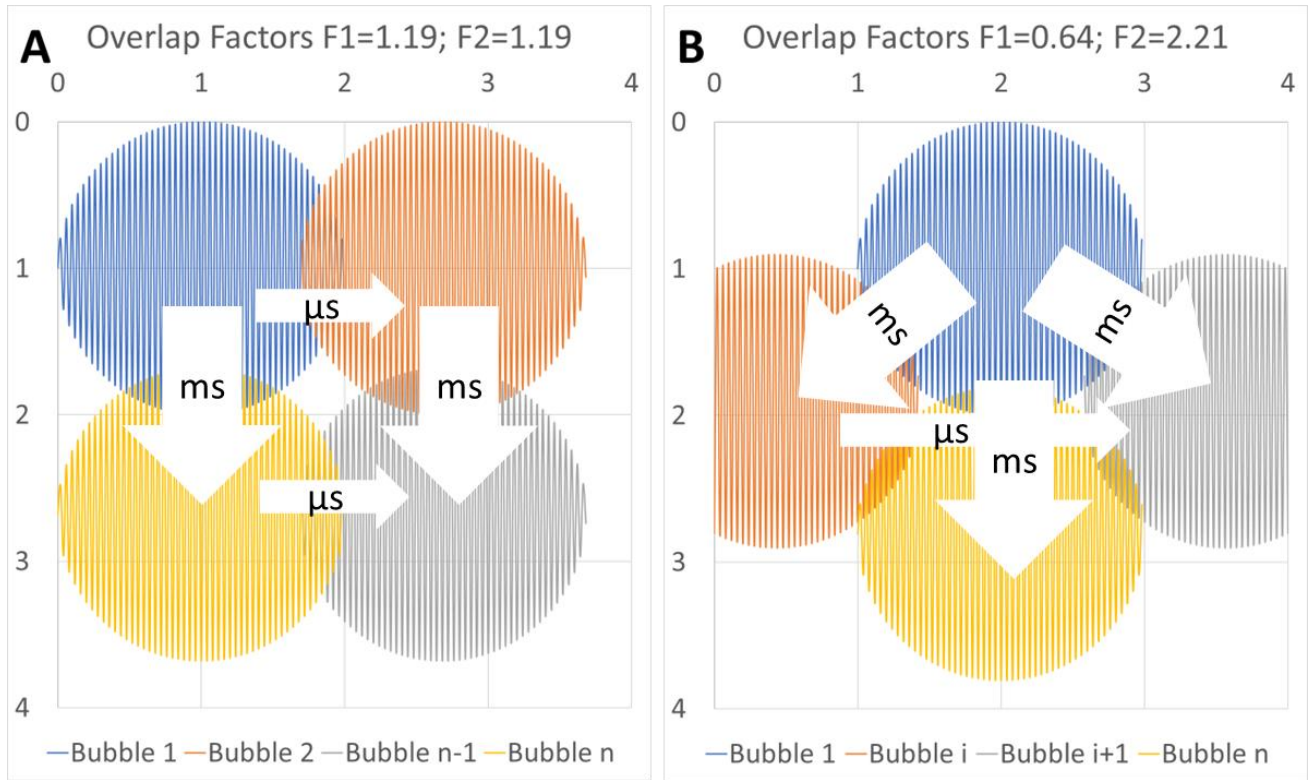
329
330
331
332
333
334
335
336

This strategy forms the basis of asymmetric spacing patterns (*Spot Distance* > *Track Distance*). Allowing larger spot spacing and even exceeding the bubble diameter can be beneficial when paired with reduced track spacing, as this compensates for the reduced overlap along the path by increasing overlap between adjacent scan lines. By minimizing consecutive spot overlap, these configurations reduce the chance of bubble interference caused by residual cavitation activity, particularly since the interpulse interval along a path is in the sub-microsecond range, which may be too short for cavitation bubbles to fully expand or dissipate. In contrast, inter-track intervals occur over milliseconds, allowing bubbles to reach full expansion before interacting with pulses from adjacent lines⁹. Therefore, avoiding spot overlaps along the scan pathway does not only act in the spatial but simultaneously in the temporal overlap domains.

337
338
339
340
341
342
343
344
345
346
347
348
349
350

This temporal separation enhances the predictability and control of tissue response as shown in the Figure 5. It is worth noting that Dose ($F1 * F2$) is the identical for both asymmetric spacing pattern (Figure 5B) and symmetric spacing pattern (Figure 5A), but asymmetry ($F2/F1$) and phase delay differs (1 vs $2 * 3^{0.5}$ and 0 vs 0.5, respectively). Although the total delivered fluence (dose, energy) remains the same, yet as evident in the Figure 5, the triangular gaps in Figure 5B are smaller than the diamond gap in Figure 5A. This geometric difference has two important implications. First, the total uncovered area in Figure 5B (the sum of the two triangular gaps) is smaller than that of the diamond-shaped gap in Figure 5A, indicating improved coverage (higher fill fraction) for the same number of pulses. Second, the area of each individual gap in Figure 5B is substantially smaller, implying reduced tissue bridge dimensions. Spatially, this suggests improved coverage and potentially easier tissue separation in the asymmetric configuration for the same pulse and treatment cumulative energy. Temporally, the reduced consecutive spot interaction combined with longer inter-track delays promotes a more gentle and efficient laser-tissue interaction. Conversely, asymmetric settings with $F2 > F1$ (spot spacing larger than track spacing) and $F1 < 1$ (non-overlapping consecutive spots) allow both improved coverage, laser-tissue interaction efficiency, and easier tissue separation at the same pulse and treatment cumulative energy, as well as equivalent outcomes at reduced cumulative energy, with continuous trade-offs between these regimes.

351
352
353



354

355 **Fig. 5** The interpulse interval along a scan path lies in the sub-microsecond range, whereas inter-track intervals occur on the
 356 millisecond scale. A) Symmetric spacing increases the likelihood of bubble interference, as it does not exploit the spatial and
 357 temporal separation domains that limit pulse–bubble interactions. B) Asymmetric spacing minimizes consecutive spot overlap,
 358 reducing bubble interference from residual cavitation activity. The longer inter-track intervals allow cavitation bubbles to fully
 359 expand and dissipate before pulses from adjacent lines arrive. Here, individual cavitation events (bubbles 1, 2, 3, ..., n) are
 360 illustrated using distinct colors to indicate their sequential generation.
 361

362 The residual gap in tissue cutting is characterized not by the nearest-neighbor spacing, but by the typical linear extent of
 363 the largest uncovered region within a unit cell. To characterize residual tissue gaps, one can introduce a characteristic void
 364 length ℓ defined as a linear measure proportional to the square root of the uncovered area fraction. Specifically, given by the
 365 expression $\ell = L\sqrt{(\pi/4)(1-\Phi)}$, where Φ is the areal fill fraction and L is the characteristic bubble projection diameter. This
 366 definition is calibrated such that square packing at kissing contact ($\Phi = \pi/4 \approx 0.79$) corresponds to $\ell/L \approx 0.414$, consistent with
 367 the diagonal extent of the central diamond-shaped void. Although ℓ does not represent the diameter of an equal-area circle, it
 368 provides a convenient and physically meaningful scaling for the linear size of residual gaps across different packing
 369 geometries. Values $\ell/L \approx 0.3-0.5$ correspond to fill fractions between approximately 75% and 90%, consistent with
 370 empirically observed conditions for effective tissue separation and the optimum window of the overlap fractions defined in this
 371 work.

372 It should be emphasized that overlap factors $F1$ and $F2$ can be regarded as universal (or generic) in a geometric and
 373 dimensional sense, not in the sense of being independent of biological or optical tissue properties. The parameters are
 374 dimensionless geometric overlap frequencies, defined as the ratio between the projected cavitation bubble diameter and the
 375 laser spot spacings along and across the scan pathway, respectively; equivalently, their reciprocals may be interpreted as
 376 normalized spacings. Owing to their dimensionless nature, these factors are applicable to any bubble size, independent of the
 377 absolute spatial scale of a given laser system, and allow direct comparison across different devices, pulse energies, and clinical
 378 platforms. While tissue biomechanics and optical properties influence the absolute bubble size, and thus the effective
 379 numerical values of $F1$ and $F2$, the underlying overlap physics is governed by these universal geometric ratios.

380 Regarding the effectiveness of asymmetric cutting and the optimized result, it would be ideal to design experiments to
 381 directly validate it, since experimental proof will always significantly increase the impact of the work. The novel task in this
 382 work is to help formally determine (from objective means) both dose and asymmetry (within optimum or at least adequate
 383 levels). The fact that all 3 aspects: (lower) pulse energy, (lower) dose, and (higher) asymmetry (positively) affect outcomes is
 384 evident and apparently universal, from previous literature.

385 Arba-Mosquera et al.²⁷ reported, aligned with other groups, that consistently in a large cohort consisting of 3 different
 386 countries, lowering the energy was one of the key factors to improve outcomes.

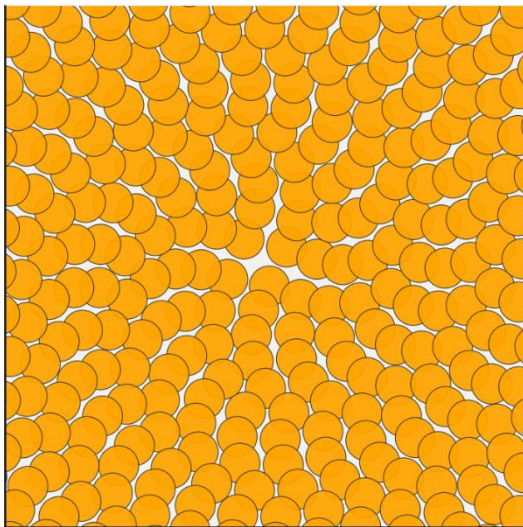
387 Arba-Mosquera et al.²⁶ mathematically modelled and demonstrated that too high energies are not consistent with minimum
 388 treatment fluence (due to the non-linear increase of bubble size with energy, i.e. above an energy range, an increase in pulse
 389 energy results in a fractional increase in bubble size, and under-proportional reduction in the required number of pulses;
 390 whereas below an energy range, a decrease in pulse energy results in a dramatic decrease in bubble size, with over-proportional
 391 increase in the required number of pulses). Further, this work interestingly opened the rigorous venue for asymmetric spacings.
 392 Using asymmetric settings, the optimum window shifts towards lower energies in a very relevant manner (without increasing
 393 the total treatment fluence). So that working with asymmetric spacings allows to effectively and safely work closer to the
 394 LIOB threshold.

395 Pradhan and Arba Mosquera²⁸ compared two ranges for pulse energies (~115nJ vs ~90nJ, with symmetric and asymmetric
 396 settings, respectively) for similar treatment fluence (~750mJ/cm²) and demonstrated that higher energies using symmetric
 397 settings provided not as good outcomes as lower pulse energies (enabled by the asymmetric spacings).

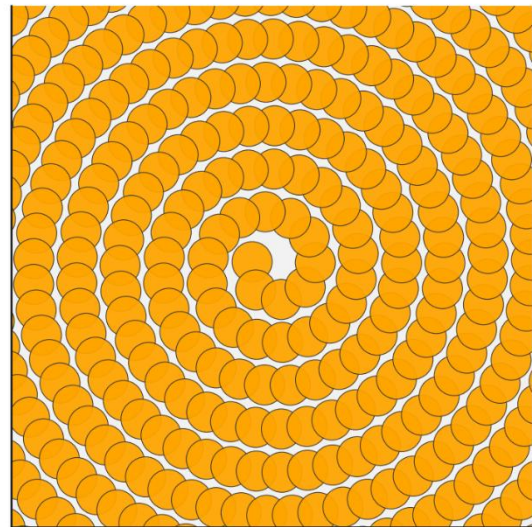
398 Theoretical models and experimental findings suggest that surface smoothness improves with well-managed bubble
 399 overlap, but this does not need to be necessarily achieved from redundant overlap along a single path. Instead, track overlap
 400 can be leveraged more efficiently, enabling a more balanced energy distribution. Amann and Arba Mosquera²⁴ explored the
 401 effects of pulse energy, spacings, and total delivered treatment energy independently using a computer modelling, reporting
 402 clear benefits in reducing pulse energy (for the same total treatment fluence); but also confirming that the asymmetric spacings
 403 were more beneficial in one than in the other direction (from a model perspective), in which consecutive pulses are placed
 404 further apart (even by distances beyond the bubble diameter, fully avoiding bubble overlap of consecutive pulses); with
 405 consecutive laps (or lines in a meander arrangement) placed tighter to maintain the total number of pulses and treatment
 406 fluence, as well as complete the overlap of the tracks for a successful separation. Further, this work allowed the inference of
 407 upper and lower levels for the required asymmetry.

408 We visually compare the asymmetric pattern (with spot distance < track distance) derived from the optimization approach
 409 used in this work, with a *reverse* asymmetric configuration in which the spot distance exceeds the track distance. Although
 410 both patterns can be designed to achieve the same nominal dose ($F1 \cdot F2 = 1.41$) their behavior in the tissue may differ. The
 411 reverse asymmetry ($F2/F1 = 0.58$) appears to produce more persistent tissue bridges and less favorable stromal smoothness
 412 compared to asymmetric pattern with $F2/F1 = 1.73$ (Fig. 6). One possible explanation for this could be that increasing the spot
 413 distance reduces beneficial intra-path overlap while shifting most of the overlap to the inter-track domain, thereby altering the
 414 spatial-temporal balance of cavitation events. While reverse asymmetry might offer practical advantages, such as potentially
 415 increasing treatment speed, its influence on bubble dynamics and tissue separation may be less optimal than that of the
 416 asymmetric spacing prescribed in this work. These observations highlight that the manner in which asymmetry is achieved
 417 may be an important parameter for cutting efficiency and interface quality.

F1=0.926, F2=1.562



F1=1.562, F2=0.926



419 **Fig. 6** Visual representation of asymmetric pulse spacing on an Archimedean spiral for a constant dose ($F1 \cdot F2 = 1.41$) with
 420 two asymmetry configurations: $F2/F1 = 1.73$ (left) and $F2/F1 = 0.58$ (right). Here, the parameters 'F1' and 'F2' are scaling
 421

factors for spot and track distance respectively. The grey contour marks the cavitation bubble boundary, and the orange fill indicates the bubble interior.

The theoretical findings are clinically supported in a large cohort analysis by Darzi, Pradhan and Arba-Mosquera²⁹ who explored reasonable ranges of pulse energies and spacings (from 75nJ to 130nJ, with symmetric and asymmetric spacings in a wide range, and treatment fluences) confirming clear trends that lower pulse energies, asymmetric spacings, and lower treatment fluences provided better outcomes. Their results suggested that maintaining a consistent dose (~12 μm^2 area assigned to a low energy pulse) achieved through asymmetric spacing such as 6.0 μm ·2.0 μm or 8.0 μm ·1.5 μm , is optimal for cutting efficiency and tissue smoothness. The requirement for overlap could be satisfied more effectively through optimized spatial and temporal distribution of pulses, rather than enforcing spot spacing to remain below bubble diameter. The integration of clinical data and predictive modeling supports the notion that decoupling spatial parameters, while controlling overall dose, enhances both tissue response and visual outcomes, providing strong empirical validation for the refined cavitation-based models proposed in earlier theoretical work^{24,26}.

Sobutas and Arba Mosquera³⁰ explored the effects of pulse energy on the treatment depth using a computer modelling with clear benefits in reducing pulse energy (for the same total treatment fluence).

Verma and Arba Mosquera⁹ introduced the plasma model and could mathematically demonstrate that for energies closer the threshold, the cavitation bubble remains constrained within the plasma volume; and only from a determined suprathreshold pulse energy are cavitation bubbles dominating the process.

Ryu et al³¹ compared using a different platform (2 different models from Carl Zeiss Meditec, VisuMax 500 and VisuMax 800) the close-to-threshold plasma KLEx (85nJ) and to a conventional low energy regime for the same platform (100nJ). Both types of treatments were performed with the same treatment fluence (625mJ/cm²). Authors reported both clinically and statistically significant differences between the two regimes. The study found that Plasma-KLEx with asymmetric spacings (*Spot Distance* > *Track Distance*), minimized microcavitation and created a lenticule with near-pure plasma, showing more favorable outcomes than Conventional-KLEx, yielding better early postoperative visual acuities and reduced induction of corneal HOAs. This study confirms the previous findings by Pradhan et. al.²⁸ using a different platform.

Park et al³² explored for a different platform the asymmetric spacings compared to a conventional symmetric spacings, both for a low energy regime (100nJ) and same treatment fluence (625mJ/cm²) and could confirm both clinically and statistically advantages for the asymmetric spacings, suggesting its universal validity.

The model presented in this work is based on several idealized assumptions, such as constant bubble size and homogeneous tissue, which inherently introduce certain limitations. Most of those limitations have been addressed in previous studies^{9,24,26}. Notably, these works demonstrated that above the optima, the variability of the bubble effects is smaller than the energy fluctuations.

The product of the overlap factors ($F1 \cdot F2$) determines the effective dose, with higher values corresponding to easier tissue dissection, whereas the ratio of the overlap factors ($F2/F1$) governs the degree of asymmetry, with larger ratios associated with reduced residual roughness. An additional constraint can be imposed such that $F2/F1 \geq F1 \cdot F2$, which implies $F1 \leq 1$ and thereby prevents spot overlap along the scan pathway independent of dose considerations. Under this framework, achieving a higher dose at the same pulse energy corresponds to an increased product ($F1 \cdot F2$), which is most effective when accompanied by greater asymmetry (see Table 4). This interplay is balanced by reducing track distances, enabling simultaneous control of dissection efficiency (dose) and surface smoothness (asymmetry). While Table 4 illustrates these relationships for a specific threshold and pulse energy, Table 5 extends the analysis across multiple threshold energies and corresponding single-pulse energies.

The Eq. (10) in our results represents the minimum dose one can apply while safely using laser energy with the highest efficiency, while Eq. (14) represents the maximum Dose for coalescence of cavitation bubbles leaving no tissue bridges. Any dose applied beyond these limits does not contribute to the physical process and is therefore redundant. The current development trend is toward lower threshold energies for cavitation bubble generation, with ~40 nJ as a representative value. Applying our method to this threshold energy allows identification of the proper optimum dose ranges. Considering minimum and maximum doses ($F1 \cdot F2 = 4/\pi$ and $F1 \cdot F2 = 2$, respectively), and applying the Photodisruption model assuming the value of K (that is the coefficient of the irradiated tissue) equal to 1.42²⁶, and a single pulse energy of 75nJ (corresponding to the Proper Optimum of the Photodisruption model), yields an optimum dose range from 441nJ to 695nJ. Using proper optimum asymmetry ($F2 / F1 = 2.62$), this leads to ideal spot and track spacings of 6.7 μm and 2.5 μm vs. 5.3 μm and 2.0 μm , for min and max doses, respectively. For the same *E_{th}* but for a single pulse energy $E_p = 55\text{nJ}$ (corresponding to the lowest Optimum of the Plasma CRT model), yields a higher optimum dose range from 570nJ to 897nJ. Using the same proper optimum asymmetry ($F2 / F1 = 2.62$), this leads to slightly tighter spot and track spacings of 5.0 μm and 1.9 μm vs. 4.0 μm and 1.5 μm , for min and max doses, respectively.

476 The precise mechanism underlying the observed reduction in surface roughness with increasing $F2/F1$ ratio (asymmetry)
 477 remains unclear. Nevertheless, previous studies consistently support this relationship from a geometrical and clinical
 478 perspective.

479 An optimization problem as this one provides for a better treatment of the localized spacing of pulses in the used lattice
 480 pattern. The findings build upon the necessary spacing to ensure pulses effectively align to a hexagonal packed array (as
 481 determined for excimer lasers³³, and leading to the asymmetry range of 1.15 to 3.46²⁴). This gives the absolute minimum
 482 number of pulses to cover a specified area for near-constant overlap. We acknowledge that this may be difficult to do
 483 practically because of the laser properties: repetition rate most notably.

484 For a constant pulse energy, increasing the track distance reduces overlap between adjacent spot pathways, leaving residual
 485 ridge patterns. Conversely, larger spot distances produce a stepwise response, as the number of pulses contributing to a single
 486 corneal location decrease; while greater overlap lowers surface roughness, it simultaneously increases the local dose. This
 487 oscillatory behavior is analogous to the Gauss's circle problem in lattice geometry, as previously described for excimer
 488 ablations³³, where the number of overlapping pulses depends on the spacing of lattice nodes relative to the spot boundary. The
 489 underlying principle remains consistent across ablation modalities. The theoretical predictions discussed here align with
 490 observed clinical transitions in commercial femtosecond systems, where spot and track spacings are being decoupled to
 491 achieve superior ablation outcomes. Furthermore, the theoretical foundations are strongly supported by clinical evidence from
 492 recent studies²⁸, directly mirroring the model's^{24,25} recommendation for maintaining a constant energy-per-area product.

493 Bohac et al.³⁴ analyzed longitudinal epithelial changes after the treatment of myopia with KLEx and the zonal change in
 494 epithelial thickness up to 12 months after SmartSight for myopic astigmatism with the SCHWIND ATOS femtosecond laser.
 495 They reported clinical outcomes in 80 eyes treated with Pulse energies ranging from 80 to 105 nJ, with a total energy dose
 496 between 440 and 583 mJ/cm². Their outcomes led to the conclusion that changes in epithelial thickness after KLEx for
 497 moderate myopia with SmartSight were minimal, indicating a low level of epithelial hyperplasia without resembling a
 498 regression-inducing lentoid. Besides these results, Spot and track settings such as $5.9 \cdot 2.9 \mu\text{m}$, $6.0 \cdot 2.1 \mu\text{m}$, $6.0 \cdot 4.4 \mu\text{m}$ or
 499 $7.6 \cdot 2.3 \mu\text{m}$ have been shown to deliver optimal stromal dissection with pulse energies as low as 75–80 nJ, corresponding to
 500 total fluences between 440 and 595 mJ/cm². These parameters yielding low total doses without compromising tissue separation
 501 are not only clinically validated, but also associated with exceptional visual and anatomical outcomes in real-world settings
 502^{35,36}. Furthermore, personal communication with experienced users of the SCHWIND ATOS system indicates that a single-
 503 pulse energy of 75 nJ combined with a spot-track setting of $7.0 \cdot 2.6 \mu\text{m}$ performs well in practice, with no perception of
 504 clinically relevant tissue bridges during dissection. Assuming a threshold energy of $E_{th} = 40 \text{ nJ}$ and a resulting bubble diameter
 505 of $4.9 \mu\text{m}$ (using $k = 1.5$ from the Photodisruption model⁹), these settings correspond to $F1 = 0.7$, $F2 = 1.9$, $F1 \cdot F2 = 1.32$, and
 506 $F2/F1 = 2.69$. These values align closely with the proper optimum identified in the present analysis, suggesting consistency
 507 between the theoretical framework and practical observations.

508 The benefits of low energy, asymmetric geometry are underscored by long-term outcome data. In a four-year retrospective
 509 study evaluating over 4000 SmartSight procedures, excellent safety and efficacy profiles were demonstrated across a wide
 510 range of myopic and astigmatic corrections. Specifically, mean uncorrected distance visual acuity (UDVA) of 20/20 or better
 511 was achieved in 91.7% of eyes, with 99.7% achieving 20/40 or better. Furthermore, 96.2% of eyes were within $\pm 0.50 \text{ D}$ of the
 512 intended spherical equivalent refraction, and only 0.2% lost one or more lines of corrected distance visual acuity (CDVA),
 513 confirming both predictability and safety over time³⁷.

514 Additional insight into the effects of asymmetric spacing and low-energy parameters is provided in studies examining the
 515 physical quality of the lenticule interface. Using *ex-vivo* and imaging analyses, researchers have shown that asymmetric, low-
 516 energy cuts produce smoother stromal surfaces and more regular lenticule geometry, compared to higher-energy or symmetric
 517 settings. Specifically, no visible tissue bridges or cavitation-related roughness were observed at the interface, and lenticule
 518 edge thickness remained well-defined and reproducible across varying cut depths and diameters³⁶. These findings suggest that
 519 asymmetric pulse geometry allows efficient tissue separation without overexposure, supporting gentle and controlled
 520 dissection. This renders the question how can the "ease of dissection" be assessed as objectively and quantitatively as possible.
 521 Different previous works determined the "ease of dissection" as a subjective cardinal score³⁸. We believe that one of the
 522 simplest objective and quantitative metrics to determine "ease of dissection" may be the required dissection time over a series
 523 of treatments³⁹. This is simple, objective, and quantitative; and allows to perform statistical comparisons for different
 524 approaches.

525 New scanning technologies for femtosecond laser ophthalmic surgery, such as multi-spot parallel scanning or strip
 526 scanning have been proposed⁴⁰. The potential applicability of these findings to those new scanning approaches can be
 527 discussed. If multi-spot parallel scanning or strip scanning set a fixed distance in one direction, then this work can provide the
 528 corridor of distances in the other direction, to balance dose and asymmetry in the best possible region. If multi-spot parallel
 529 scanning or strip scanning sets a distance range of selectable distances in one direction, then this work can provide the range of
 530 corridor of distances in the other direction, to balance dose and asymmetry in the best possible region. If multi-spot parallel

scanning or strip scanning provides fully selectable distances in one direction, then this work can provide the full range of distances in the other direction, to balance dose and asymmetry in the best possible region. Based on these considerations, a practical framework compatible with emerging multi-spot or parallel scanning systems can be outlined. First, the optimum pulse energy should be identified, typically around $1.7 \cdot Eth$, from which the corresponding bubble size can be inferred. The optimum total dose ($F2 \cdot F2$) may then be selected within identified optimum ranges of 1.3–1.6, and the asymmetry ratio ($F2/F1$) within identified optimum ranges of 2–3.5. Once these parameters are defined, the spot distance can remain fixed to avoid overlap along the pathway, while the dose can be modulated solely by adjusting the track distance. This approach allows energy and spot spacing to remain near their optimal values, while treatment efficiency and tissue separation quality are fine-tuned through a single parameter, track distance, constrained within well-defined limits.

All findings presented in this work are derived from geometric analyses, with no explicit treatment of the temporal domain. Nonetheless, the geometrical principles are consistent with and reinforced by temporal considerations, which we address here.

Bubble dynamics remain a source of uncertainty, as validated estimates of cavitation bubble collapse time in the living cornea are lacking. Reported values vary from ~8–10 μ s for sub- μ J energies in water to ~1 ms for multi- μ J pulse energies in ex vivo corneas^{41,42}. Based on available data, we reasonably assume that bubble lifetime in the cornea is <1 ms, scales with bubble size (and thus pulse energy), and is shorter than in water due to the higher substrate fraction. For low pulse energies near threshold, bubbles typically undergo a single expansion–collapse cycle. With low energies (<100 nJ), lifetimes in the cornea are likely even shorter (<8 μ s), reinforcing the benefits of temporal separation.

For a given dose, asymmetric pulse arrangements, where pulses are closely packed along the spot pathway but tracks are more widely separated (e.g., ELITA, Z8, Johnson & Johnson Surgical Vision, Inc) result in overlapping pulses separated by sub-microsecond intervals (MHz repetition rates), while overlaps between tracks occur over milliseconds. Under these conditions, consecutive pulses interact within the lifetime of cavitation bubbles, limiting their maximum expansion and creating mutual interference. In symmetric configurations (e.g., VisuMax, Carl Zeiss Meditec AG.), both spot and track distances are equal, so pulse-to-pulse overlap remains at the microsecond scale and track overlaps is in the order of milliseconds, again preventing full bubble development. In contrast, in asymmetric settings (e.g. SCHWIND ATOS, SCHWIND eye-tech solutions GmbH.), where spot distance greatly exceeds track distance, create non-overlapping pulses (μ s separation) but overlapping tracks at millisecond intervals. This allows cavitation bubbles to reach their maximum effect without interference from subsequent pulses. The difference across settings spans more than three orders of magnitude (>1000 \times) in overlap timing, which makes a critical distinction in tissue response.

Under optimal asymmetric spacing, overlaps occur on the millisecond scale, well beyond the bubble lifetime (<10 μ s), which minimizes destructive pulse–bubble interactions. These considerations support the view that optimal surgical parameters represent a “sweet spot” balancing laser stress, mechanical stress, and surface smoothness. Our theoretical findings align with prior reports linking dissection quality, occurrence of OBLs, and visual recovery to laser settings^{24,36,37}. Specifically, surface smoothness improves with lower pulse energy, tighter track distances, and increased asymmetry (especially above a 2:1 ratio). Laser stress decreases with reduced energy, larger spacing, and higher asymmetry by limiting bubble overlap. Mechanical stress, in turn, is minimized within the asymmetry range of ~1.15–3.46, where energy distribution balances cutting efficiency with tissue integrity.

There are other considerations which may benefit from the proposed strategy. For example, larger heating effects can cause a problem. For instance, separating the pulses with some form of a regionalized Sobol sampling can reduce cumulative heat load in one area, while still having asymmetry. At this regard, both using (close to) minimum dose as well as using asymmetric spacings with *Spot Distance* > *Track Distance*, both are independent simple measures to reduce heating. Actually, both together act synergistically by reducing the total energy deposition while non overlapping consecutive pulses; and still ensuring (facilitating) tissue bridge-free dissections.

Early visual recovery appears to depend more on minimizing laser and mechanical stress than on surface roughness alone. While smoother corneal interfaces predictably enhance vision, they also accelerate epithelial remodeling by providing a better baseline. Thus, reducing energy deposition and bubble interference may be more critical for POD1 outcomes than further minimizing residual roughness, though both factors contribute. In practice, low pulse energy with spot distances slightly larger than bubble size (avoiding spatial/temporal overlap along the pathway) and tight track distances creates the most favorable balance.

There are potential refinements to this work. On the one hand, we calculated the number of pulses based on the area of a flat disc. This may be refined to account for the true cutting surface resembling something between a spherical cap and a parabolic dish (enlarging the treatment area respect to the disc). Further, one may account for the compression and deformation of the tissue under the contact element during the laser process⁴³. But both these refinements do not change the presented findings, since the treatment area cancels out in the calculation of dose (Eqs 1-3).

We have used the photodisruption model in this work, and not the more recently introduced plasma model⁹ which is less commonly applied so far. Earlier work based on this model proposes that the maximum surface smoothness is achieved at an

infinite overlap ($F = \infty$, infinite dose = maximum smoothness), with $F = 1.41$ as the smallest factor permitting bridge-free dissection, and $F = 1.19$ as a reasonable compromise. In that work, we assumed symmetric conditions ($F1 = F2$). In asymmetric configurations, however, $F1$ and $F2$ can be selected independently, constrained by $F1 \cdot F2 \approx 1.41$ as a practical compromise between $F1 \cdot F2 = 2$ for a bridge free tissue dissection, and $F1 \cdot F2 = 1.27 (= 4/\pi)$ for the minimum dose. Furthermore, an asymmetry ratio $F2/F1 > 2$ is shown to effectively reduce roughness. This yields, for example, $F1 \approx 0.73$ (*Spot Distance* $\approx 1.4 \cdot$ *Bubble Diameter*) and $F2 \approx 1.92$ (*Track Distance* $\approx 0.52 \cdot$ *Bubble Diameter*), corresponding to the proper optimum solution determined in this study (dose ($F1 \cdot F2$) of 1.41 and asymmetry ratio ($F2/F1$) of 2.62). More broadly, we propose a spot spacing range of 100–165% of bubble diameter, with track distances adjusted accordingly, as the geometric–temporal “sweet spot” for femtosecond laser refractive procedures. The presented findings may provide a foundation for future system designs to incorporate and expand upon these concepts.

5. Conclusion

The bubble overlap denoted by the scaling factors $F1$ and $F2$ plays a pivotal role in determining cutting smoothness and efficiency. Extending our previous works, an optimum window for the overlap factors has been defined, which optimizes overall dose per treatment and minimizes corneal surface roughness. Collectively, the clinical and biomechanical data confirm that spot spacings above $5 \mu\text{m}$, when used in conjunction with lower pulse energies and asymmetric spacing, provide a robust foundation for safe, efficient, and high-quality corneal refractive surgery. A general consensus has emerged among femtosecond laser platform users that the ‘sweet-spot’ energy density for currently available commercial systems lies in the range of 400-500 mJ/cm^2 . A proper optimum to achieve this energy density can vary slightly between clinical settings but increasingly shows a trend towards increased spot and track distance asymmetry, reduced pulse energy leading to a reduced dose, suggesting that the currently recognized “sweet-spot” energy density will further reduce as the technology evolves. The alignment of empirical results with theoretical models justifies the growing clinical trend toward dose-preserving, low-energy, asymmetric ablation paradigms in modern lenticule extraction.

Acknowledgments

None

Funding

Not Applicable

Conflicts of interest

The authors are employees of SCHWIND eye-tech solutions GmbH, Germany. The authors declare that there are no financial interests, commercial affiliations, or other potential conflicts of interest that could have influenced the objectivity of this research or the writing of this paper” is included in a Disclosures section of the manuscript.

Data availability statement

This article has no associated data generated

Author contribution statement

Conceptualization, SAM and SV; Methodology, SAM and SV; Software, N/A.; Validation, N/A; Formal Analysis, SAM and SV; Investigation, SAM and SV; Resources, N/A; Data Curation, N/A; Writing – Original Draft Preparation, SV; Writing – Review & Editing, SAM and SV; Visualization, SAM and SV; Supervision, SAM; Project Administration, SAM; Funding Acquisition, N/A.

- 624 1. A. Saad et al., “Refractive outcomes of small lenticule extraction (SMILE) Pro® with a 2 MHz femtosecond laser,” *Int*
625 *Ophthalmol* **44**(1), 52 (2024) [doi:10.1007/s10792-024-02915-2].
- 626 2. K. R. Pradhan and S. Arba Mosquera, “SmartSight Correction of Compound Myopic Astigmatism Treatments With
627 Preoperative Astigmatism > 1.00 Diopter Using the SCHWIND ATOS: A Retrospective Case Series,” *J Refract Surg*
628 **40**(5), e328–e335 (2024) [doi:10.3928/1081597X-20240415-02].
- 629 3. P. Teng et al., “Acoustic studies of the role of immersion in plasma-mediated laser ablation,” *IEEE Journal of Quantum*
630 *Electronics* **23**(10), 1845–1852 (1987) [doi:10.1109/JQE.1987.1073233].
- 631 4. M. H. Niemz, E. G. Klancnik, and J. F. Bille, “Plasma-mediated ablation of corneal tissue at 1053 nm using a Nd:YLF
632 oscillator/regenerative amplifier laser,” *Lasers Surg Med* **11**(5), 426–431 (1991) [doi:10.1002/lsm.1900110507].
- 633 5. D. Aron-Rosa et al., “Use of the neodymium-YAG laser to open the posterior capsule after lens implant surgery: a
634 preliminary report,” *J Am Intraocul Implant Soc* **6**(4), 352–354 (1980) [doi:10.1016/s0146-2776(80)80036-x].
- 635 6. M. M. Krasnov, “Laseropuncture of anterior chamber angle in glaucoma,” *Am J Ophthalmol* **75**(4), 674–678 (1973)
636 [doi:10.1016/0002-9394(73)90819-2].
- 637 7. D. Z. Reinstein et al., “Accuracy and reproducibility of artemis central flap thickness and visual outcomes of LASIK with
638 the Carl Zeiss Meditec VisuMax femtosecond laser and MEL 80 excimer laser platforms,” *J Refract Surg* **26**(2), 107–119
639 (2010) [doi:10.3928/1081597X-20100121-06].
- 640 8. N. Tinne et al., “Effects of cavitation bubble interaction with temporally separated fs-laser pulses,” *J Biomed Opt* **19**(4),
641 048001 (2014) [doi:10.1117/1.JBO.19.4.048001].
- 642 9. S. Verma and S. Arba Mosquera, “A Refined Model for Ablation Through Cavitation Bubbles with Ultrashort Pulse
643 Lasers,” *11, Photonics* **11**(11), 1047, Multidisciplinary Digital Publishing Institute (2024)
644 [doi:10.3390/photonics11111047].
- 645 10. A. Vogel et al., “Mechanisms of femtosecond laser nanosurgery of cells and tissues,” *Applied Physics B: Lasers and*
646 *Optics* **81**, 1015–1047, Springer (2005) [doi:10.1007/s00340-005-2036-6].
- 647 11. T. Juhasz et al., “Corneal refractive surgery with femtosecond lasers,” *IEEE Journal of Selected Topics in Quantum*
648 *Electronics* **5**(4), 902–910 (1999) [doi:10.1109/2944.796309].
- 649 12. H. B. Dick, M. Elling, and A. Willert, “Femtosecond laser in ophthalmology – A short overview of current applications,”
650 *Medical Laser Application* **25**(4), 258–261 (2010) [doi:10.1016/j.mla.2010.07.005].
- 651 13. A. A. Farjo et al., “Femtosecond lasers for LASIK flap creation: a report by the American Academy of Ophthalmology,”
652 *Ophthalmology* **120**(3), e5–e20 (2013) [doi:10.1016/j.ophtha.2012.08.013].
- 653 14. I. Ratkay-Traub et al., “Ultra-short pulse (femtosecond) laser surgery: initial use in LASIK flap creation,” *Ophthalmol*
654 *Clin North Am* **14**(2), 347–355, viii–ix (2001).
- 655 15. S. Freidank, A. Vogel, and N. Linz, “Mechanisms of corneal intrastromal laser dissection for refractive surgery: ultra-
656 high-speed photographic investigation at up to 50 million frames per second,” *Biomed Opt Express* **13**(5), 3056–3079
657 (2022) [doi:10.1364/BOE.455926].
- 658 16. K. G. Stonecipher et al., “Laser in situ keratomileusis flap complications and complication rates using mechanical
659 microkeratomes versus femtosecond laser: Retrospective review,” *Medical Research Archives* **2**(3) (2015).
- 660 17. N. Tinne et al., “Interaction Mechanisms of Cavitation Bubbles Induced by Spatially and Temporally Separated fs-Laser
661 Pulses,” *PLoS One* **9**(12), e114437 (2014) [doi:10.1371/journal.pone.0114437].
- 662 18. H. Minoguchi, M. Teus, and H. Fu, *Atomic force microscopy and scanning electron microscopy for characterization of*
663 *interface surface roughness after ELITA femtosecond laser treatments* (2024) [doi:10.21203/rs.3.rs-4934376/v1].
- 664 19. S. Mian, O. Abbasi, and T. Juhasz, “Femtosecond laser-assisted posterior lamellar keratoplasty: Initial studies of surgical
665 technique in eye bank eyes,” *Ophthalmology* **112**, 44–49 (2005) [doi:10.1016/j.ophtha.2004.06.037].
- 666 20. N. Tinne et al., “Interaction dynamics of spatially separated cavitation bubbles in water,” *J Biomed Opt* **15**(6), 068003
667 (2010) [doi:10.1117/1.3526366].
- 668 21. “The influence of a spatial and temporal pulse-overlap on the laser-tissue-interaction of modern ophthalmic laser systems |
669 Request PDF,” <[https://www.researchgate.net/publication/235217558_The_influence_of_a_spatial_and_temporal_pulse-](https://www.researchgate.net/publication/235217558_The_influence_of_a_spatial_and_temporal_pulse-overlap_on_the_laser-tissue-interaction_of_modern_ophthalmic_laser_systems)
670 [overlap_on_the_laser-tissue-interaction_of_modern_ophthalmic_laser_systems](https://www.researchgate.net/publication/235217558_The_influence_of_a_spatial_and_temporal_pulse-overlap_on_the_laser-tissue-interaction_of_modern_ophthalmic_laser_systems)> (accessed 22 September 2025).
- 671 22. T. Schultz et al., “Greater vertical spot spacing to improve femtosecond laser capsulotomy quality,” *J Cataract Refract*
672 *Surg* **43**(3), 353–357 (2017) [doi:10.1016/j.jcrs.2016.12.028].
- 673 23. M. Lombardo et al., “Surface quality of femtosecond dissected posterior human corneal stroma investigated with atomic
674 force microscopy,” *Cornea* **31**(12), 1369–1375 (2012) [doi:10.1097/ICO.0b013e31823f774c].
- 675 24. H. Amann and S. Arba Mosquera, “Optimization of the Spot Spacings for Reducing Roughness in Laser-Induced Optical
676 Breakdown Processes for Corneal Laser Vision Correction,” *2, Photonics* **11**(2), 114, Multidisciplinary Digital Publishing
677 Institute (2024) [doi:10.3390/photonics11020114].

- 678 25. S. Arba-Mosquera and S. Verma, “Analytical optimization of the ablation efficiency at normal and non-normal incidence
679 for generic super Gaussian beam profiles,” *Biomed Opt Express* **4**(8), 1422–1433 (2013) [doi:10.1364/BOE.4.001422].
- 680 26. S. Arba-Mosquera et al., “Analytical optimization of the cutting efficiency for generic cavitation bubbles,” *Biomed Opt*
681 *Express* **12**(7), 3819–3835 (2021) [doi:10.1364/BOE.425895].
- 682 27. S. Arba-Mosquera et al., “Influence of Extrinsic and Intrinsic Parameters on Myopic Correction in Small Incision
683 Lenticule Extraction,” *J Refract Surg* **35**(11), 712–720 (2019) [doi:10.3928/1081597X-20191003-01].
- 684 28. K. R. Pradhan and S. Arba Mosquera, “Comparing high and low energy outcomes on day one for SmartSight myopic-
685 astigmatism treatments with the SCHWIND ATOS: a retrospective case series,” *BMC Ophthalmol* **23**, 328 (2023)
686 [doi:10.1186/s12886-023-03076-z].
- 687 29. S. Darzi, K. R. Pradhan, and -Mosquera Samuel Arba, “Enhancing Predicted Visual Acuity After SmartSight Lenticule
688 Extraction: Identifying Key Factors With Machine Learning,” *Journal of Refractive Surgery* **40**(12), e974–e984, SLACK
689 Incorporated (2024) [doi:10.3928/1081597X-20241030-01].
- 690 30. S. Sobutas and S. Arba Mosquera, “Model of the Effects of Femtosecond Laser Pulse Energy on the Effective Z-Position
691 of the Resulting Cut after Laser-Induced Optical Breakdown,” *Photonics* **11**(8), 685, Multidisciplinary Digital Publishing
692 Institute (2024) [doi:10.3390/photonics11080685].
- 693 31. S. Ryu et al., “Optimizing Plasma Formation and Minimizing Microcavitation to Enhance Clinical Outcomes in
694 Keratorefractive Lenticule Extraction,” *J Refract Surg* **41**(7), e635–e644 (2025) [doi:10.3928/1081597X-20250509-05].
- 695 32. E. S. Park et al., “Reducing higher-order aberrations after keratorefractive lenticule extraction using asymmetric spacing
696 spot/track distances with low-energy levels,” *J Cataract Refract Surg* **51**(10), 895–902 (2025)
697 [doi:10.1097/j.jcrs.0000000000001713].
- 698 33. “Optimum Laser Beam Characteristics for Achieving Smoother Ablations in Laser Vision Correction | IOVS | ARVO
699 Journals,” <<https://iovs.arvojournals.org/article.aspx?articleid=2617370>> (accessed 26 September 2025).
- 700 34. M. Boháč et al., “Epithelial Remodelling in Myopia After Keratorefractive Lenticule Extraction,” *Ophthalmol Ther* **14**(6),
701 1237–1247 (2025) [doi:10.1007/s40123-025-01138-7].
- 702 35. I. Gabric, K. R. Pradhan, and S. Arba Mosquera, “Unique Features of the ATOS Laser for Lenticule Extraction:
703 Programming, Intraoperative Software Use, and Dissection Techniques,” in *Femtosecond Laser Assisted Lenticule*
704 *Extraction: Principles, Techniques, Complication Management, and Future Concepts in KLEx*, W. Sekundo and F. M.
705 Wagner, Eds., pp. 339–347, Springer Nature Switzerland, Cham (2024) [doi:10.1007/978-3-031-60424-9_24].
- 706 36. K. Pradhan and S. Arba Mosquera, “Lenticule and Interface Properties and Geometries in SmartSight®,” pp. 329–338
707 (2024) [doi:10.1007/978-3-031-60424-9_23].
- 708 37. K. R. Pradhan et al., “Clinical Results of SmartSight in Four Years Experience,” in *Femtosecond Laser Assisted Lenticule*
709 *Extraction: Principles, Techniques, Complication Management, and Future Concepts in KLEx*, W. Sekundo and F. M.
710 Wagner, Eds., pp. 349–369, Springer Nature Switzerland, Cham (2024) [doi:10.1007/978-3-031-60424-9_25].
- 711 38. S. Taneri et al., “Results of thin-cap small-incision lenticule extraction,” *J Cataract Refract Surg* **47**(4), 439–444 (2021)
712 [doi:10.1097/j.jcrs.0000000000000470].
- 713 39. S. Brar, S. Ganesh, and S. Bhargav, “Comparison of Intraoperative Time Taken for Docking, Lenticule Dissection, and
714 Overall Workflow for SMILE Performed With the VisuMax 800 Versus the VisuMax 500 Femtosecond Laser,” *J Refract*
715 *Surg* **39**(9), 648 (2023) [doi:10.3928/1081597X-20230726-03].
- 716 40. H. Li et al., “Multi-focus non-periodic scanning method for femtosecond lasers based on DMD and galvanometer
717 scanners [Invited],” *Chin. Opt. Lett.*, COL **22**(5), 051701, Chinese Optical Society (2024) [doi:10.1364/COL.22.051701].
- 718 41. N. Tinne et al., “Interaction Mechanisms of Cavitation Bubbles Induced by Spatially and Temporally Separated fs-Laser
719 Pulses,” *PLoS One* **9**(12), e114437 (2014) [doi:10.1371/journal.pone.0114437].
- 720 42. T. Juhasz et al., “Time-resolved observations of shock waves and cavitation bubbles generated by femtosecond laser
721 pulses in corneal tissue and water,” *Lasers Surg Med* **19**(1), 23–31 (1996) [doi:10.1002/(SICI)1096-
722 9101(1996)19:1%3C23::AID-LSM4%3E3.0.CO;2-S].
- 723 43. T. Kehrer and S. Arba Mosquera, “A simple cornea deformation model,” *Advanced Optical Technologies* **10**(6), 433–450
724 (2021) [doi:10.1515/aot-2021-0039].
- 725